applied sciences

MDPI

Article

Histopathological Image Analysis Using Machine Learning to Evaluate Cisplatin and Exosome Effects on Ovarian Tissue in Cancer Patients

Tuğba Şentürk [1,*], Fatma Latifoğlu [2,*], Çiğdem Gülüzar Altıntop [2], Arzu Yay [3], Zeynep Burçin Gönen [4], Gözde Özge Önder [3], Özge Cengiz Mat [3] and Yusuf Özkul [5]

[1] Department of Biomedical Engineering, İnonu University, Malatya 44280, Türkiye
[2] Department of Biomedical Engineering, Erciyes University, Kayseri 38039, Türkiye; cigdemacer@erciyes.edu.tr
[3] Department of Histology and Embryology, Faculty of Medicine, Erciyes University, Kayseri 38039, Türkiye; arzuyay@erciyes.edu.tr (A.Y.); gozdekorkmaz@erciyes.edu.tr (G.Ö.Ö.); ozgemat@erciyes.edu.tr (Ö.C.M.)
[4] Department of Oral and Maxillofacial Surgery, Genome and Stem Cell Centre, Erciyes University, Kayseri 38039, Türkiye; zeynepburcin@erciyes.edu.tr
[5] Department of Medical Genetics, Faculty of Medicine, Erciyes University, Kayseri 38039, Türkiye; ozkul@erciyes.edu.tr
* Correspondence: tugba.senturk@inonu.edu.tr (T.Ş.); flatifoglu@erciyes.edu.tr (F.L.)

Abstract: Cisplatin, a widely used chemotherapeutic agent, is highly effective in treating various cancers, including ovarian and lung cancers, but it often causes ovarian tissue damage and impairs reproductive health. Exosomes derived from mesenchymal stem cells are believed to possess reparative effects on such damage, as suggested by previous studies. This study aims to evaluate the reparative effects of cisplatin and exosome treatments on ovarian tissue damage through the analysis of histopathological images and machine learning (ML)-based classification techniques. Five experimental groups were examined: Control, cisplatin-treated (Cis), exosome-treated (Exo), exosome-before-cisplatin (ExoCis), and cisplatin-before-exosome (CisExo). A set of 177 Local Binary Pattern (LBP) features were extracted from histopathological images, followed by feature selection using Lasso regression. Classification was performed using ML algorithms, including decision tree (DT), k-nearest neighbors (KNN), support vector machine (SVM), and Artificial Neural Network (ANN). The CisExo group exhibited the most homogeneous texture, suggesting effective tissue recovery, whereas the ExoCis group demonstrated greater heterogeneity, possibly indicating incomplete recovery. KNN and ANN classifiers achieved the highest accuracy, particularly in comparisons between the Control and CisExo groups, reaching an accuracy of 87%. The highest classification accuracy was observed for the Control vs. Cis groups (approximately 91%), reflecting distinct features, whereas the Control vs. Exo groups demonstrated lower accuracy (around 68%) due to feature similarity. Exosome treatments, particularly when administered post-cisplatin, significantly improve ovarian tissue recovery. This study highlights the potential of ML-based classification as a robust tool for evaluating therapeutic outcomes. Additionally, it underscores the promise of exosome therapy in mitigating chemotherapy-induced ovarian damage and preserving reproductive health. Further research is warranted to validate these findings and optimize treatment protocols.

Keywords: cisplatin; exosome; local binary pattern; k-nearest neighbors; support vector machine; artificial neural network; decision tree

Academic Editors: Gang Wei and Pedro Couto

Received: 18 December 2024
Revised: 5 February 2025
Accepted: 12 February 2025
Published: 14 February 2025

Citation: Şentürk, T.; Latifoğlu, F.; Altıntop, Ç.G.; Yay, A.; Gönen, Z.B.; Önder, G.Ö.; Mat, Ö.C.; Özkul, Y. Histopathological Image Analysis Using Machine Learning to Evaluate Cisplatin and Exosome Effects on Ovarian Tissue in Cancer Patients. *Appl. Sci.* **2025**, *15*, 1984. https://doi.org/10.3390/app15041984

1. Introduction

Cancer is one of the leading causes of death worldwide, characterized by the uncontrolled division and proliferation of cells due to genetic and environmental factors, ultimately leading to tumor formation [1,2]. Over 100 types of cancer affect the human body, and different treatment methods are applied for each type of cancer, one of which is cytotoxic (chemotherapy) treatment. Although this method is effective for treating many types of cancer, it causes numerous side effects in the body. These side effects primarily affect rapidly dividing cells such as blood cells, gastrointestinal system cells, hair follicles, and reproductive organs. While cytotoxic chemotherapy used in cancer treatment achieves successful results in prolonging survival, it significantly reduces post-treatment quality of life, particularly due to its devastating effects on female reproductive health. Therefore, developing new approaches to mitigate the side effects of cisplatin is critically important.

When cytotoxic chemotherapy is applied to premenopausal women, it can lead to follicular destruction, ovarian fibrosis, premature ovarian failure, reduced estrogen and progesterone levels, and an increased risk of infertility [3,4]. The likelihood of infertility is associated with factors such as the patient's age, drug dosage, treatment duration, and combinations of cytotoxic chemotherapy agents [3,5]. These drugs are also known to be both teratogenic (causing abnormalities in exposed fetuses) and mutagenic (inducing mutations in genetic material), thereby possessing a high potential for adverse effects [5–7].

Cytotoxic chemotherapy, with cisplatin (Cis, cis-diamminedichloroplatinum-II) being one of the most commonly used agents, is effectively utilized in various types of cancers, including head and neck, testicular, ovarian, bladder, and small-cell lung cancers [8,9]. Although the exact mechanism of cisplatin's toxic effects on the ovaries remains unclear, it is suggested that increased production of reactive oxygen species and decreased antioxidant levels contribute to its toxicity [10,11]. The effects of chemotherapy on the female reproductive system include oocyte damage and apoptosis around follicles, which may lead to premature ovarian failure [12]. Cisplatin can cause double-strand DNA damage, triggering apoptosis in granulosa cells and oocytes, thereby negatively impacting the follicular reserve in women. This highlights the critical need for innovative strategies to protect reproductive reserves during chemotherapy [13]. Numerous studies suggest that antioxidant therapy has the potential to prevent cisplatin-induced ovarian toxicity and the infertility resulting from this toxicity. Notably, mesenchymal stem cells (MSCs) have garnered significant attention in recent years due to their therapeutic capabilities and roles in damage repair. Multipotent stem cells derived from human umbilical cords (huMSCs) offer several advantages, including high self-renewal capacity, low immunogenicity, ease of accessibility, and wide availability [14]. Additionally, it has been demonstrated that huMSCs enhance ovarian reserve function [15]. Exosomes secreted by MSCs play a critical role in tissue regeneration and repair processes, as supported by numerous studies [16]. These exosomes exhibit functions such as reducing inflammation, modulating immune responses, and supporting tissue repair. Moreover, exosomes are reported to carry miRNAs that may influence cancer suppression or progression without posing a tumor formation risk [16–18]. Given these advantages, exosomes are considered a suitable option for clinical applications due to their low immunogenicity, lack of tumorigenic potential, and minimal ethical risks, making them a favorable alternative in therapeutic settings [15].

A review of the literature reveals that the effects of cisplatin on ovarian morphology have been examined in many studies. Renard et al. investigated the effects of simultaneous exposure to cisplatin and the electromagnetic environment of clinical magnetic resonance imaging (MRI) on the in vitro chemotherapy sensitivity of ovarian cancer cell lines [19]. In their study, cells treated with cisplatin were exposed to three MRI acquisition sequences produced by a 3T clinical device—T2-weighted 2D turbo spin echo, 3D TSE,

and gradient recalled echo (GRE)—to examine the effects of radiofrequency (RF) fields and time-varying magnetic fields using methods previously employed by Schweizer and colleagues [20]. The analysis concluded that simultaneous exposure to cisplatin and MRI did not significantly affect the in vitro activity (cisplatin effect) on ovarian cancer cell lines. Kun Hsing Yu et al. [21] analyzed histopathology slides, RNA-Seq, and proteomic data from 587 patients with primary serous ovarian adenocarcinoma who participated in The Cancer Genome Atlas (TCGA) and Genomic Data Commons studies [22]. They developed a systematic algorithm to integrate histopathology and functional omics findings and predict patient responses to platinum-based chemotherapy. To reduce the risk of overfitting, the architectures AlexNet [23], GoogLeNet [24], and VGGNet [25] pretrained with weights from the ImageNet dataset were used to create classification models with histopathological images containing tumor cells. Kun Hsing Yu and colleagues achieved approximately 95% accuracy in identifying cancerous regions and classified tumor grades with about 80% accuracy. Ruilin Lei et al. [26] aimed to develop a deep learning model to predict the platinum sensitivity of epithelial ovarian cancer patients based on contrast-enhanced MRI. Their team collected images from 93 patients who underwent contrast-enhanced MRI and received cisplatin/carboplatin chemotherapy at Sun Yat-sen Memorial Hospital. In total, 62 images were used as the training group and 31 images were set aside for validation. Two different deep learning models were utilized: the first, a primary tumor model, used tumor images obtained from volume of interest (VOI) segmentation of the entire image; the second used the entire abdominal images fed into the architecture of a pretrained 3D ResNet network. After extracting features from the relevant VOIs, Principal Component Analysis (PCA) was applied to reduce data dimensions. A support vector machine was then used on the PCA-generated data to classify the likelihood of cisplatin sensitivity, demonstrating that the full abdominal model performed better than the primary tumor model [26]. Studies have shown that convolutional neural networks (CNNs) can accurately identify cancerous regions in ovarian tissues with high AUC values and effectively classify tumor grades [27]. Wenqing et al. [28] conducted a study to analyze the feature extraction performance of deep structured algorithms in diagnosing lung nodules on computer tomography (CT) images and compared it to computer-aided diagnostic (CADx) systems. From 1018 cases of diagnostic and lung cancer screening thoracic CT scans containing marked and annotated lesions, they generated three images for each segmented grayscale ROI fragment: the original ROI containing areas surrounding nodules, the nodule-only image, and a degraded image. These were combined into a Red–Green–Blue (RGB) channel resulting in 134,668 samples. They extracted features by designing CNN, deep belief network (DBN), and stacked denoising auto-encoder (SDAE) algorithms and created a new three-channel image generation method for nodule diagnosis. They also compared AlexNet-based transfer learning in this experiment by training the last 1–3 layers. Wenqing et al. [28] concluded that compared to traditional CADx systems, deep learning algorithms did not exhibit biases observed in misclassified data. They analyzed that the deep learning-based computerized lung nodule diagnostic scheme could distinguish malignant from benign lung nodules with a relatively higher AUC of 0.899 ± 0.018.

The classification and identification of ovarian masses remain challenging due to the complexity of image backgrounds [29]. This study utilized the Gray-Level Co-Occurrence Matrix (GLCM) and Tamura texture features to classify ovarian abnormalities. Various texture features such as coarseness, contrast, directionality, and roughness were extracted, and a classifier resembling Light Glioblastoma (GBM) was employed for analysis. The classification results showed that combining GLCM and Tamura texture features, even without segmentation, achieved an accuracy rate of 72%. Chi-Ling Huang et al. [30] demonstrated the importance of determining cisplatin (CP) resistance, particularly for ovarian adenocar-

cinoma cells. GLCM features were extracted from images to characterize textures. Ovarian carcinoma cell lines of serous type (OVCAR-4 and A2780) and clear cell type (IGROV1) with CP resistance were used to demonstrate GLCM texture feature extraction from images. The signal-to-noise ratio was employed to evaluate the chemoresistance grade of cell images derived from GLCM texture feature extraction. The differences between wild-type and CP-resistant cells were statistically significant in all cases ($p < 0.001$). GLCM-based in vitro and ex vivo feature extraction reliably identified CP-resistant ovarian adenocarcinoma cells.

This study investigates the histopathological damage caused by cisplatin, a commonly used chemotherapeutic agent, on the female reproductive system—particularly ovarian tissues. It also evaluates the potential restorative effects of exosome application on this damage. Although cisplatin is successfully employed in the treatment of various cancer types due to its chemotherapeutic efficacy, it can cause significant side effects to female reproductive health. In this context, understanding the potential reparative effects of exosome application on cisplatin-induced damage holds critical importance for the development of treatment approaches. The effects of cisplatin and exosome applications on ovarian tissues were evaluated using advanced analytical methods. Local Binary Pattern (LBP) features were initially extracted from ovarian histopathological images. These features were then analyzed across four distinct classes: Cisplatin–Control (Cis–Control), Cisplatin+Exosome–Control (Cis+Exo–Control), Exosome+Cisplatin–Control (Exo-Cis–Control), and Exosome–Control (Exo–Control). These classes were designed to investigate the effects of cisplatin and exosome applications on ovarian tissues, and classification was performed using machine learning algorithms.

The literature contains limited comprehensive studies aiming to mitigate the side effects of cisplatin on ovarian tissues through exosome applications. This study addresses this gap by integrating image processing and machine learning methods to present a novel approach. It provides a comprehensive analysis of both the damage caused by cisplatin alone and the potential reparative effects of exosomes on this damage.

The highlights of the study:

- Damage to ovarian tissues: A detailed analysis of the histopathological effects of cisplatin was conducted.
- Restorative effect of exosomes: The potential therapeutic effects of exosome applications were examined.
- Integration of machine learning and image processing: A novel approach was presented to classify the effects of different applications using these methods.
- Comprehensive analysis: Cisplatin and exosome applications were analyzed both individually and in combination, providing new insights for treatment strategy.
- Accuracy: The images are manually classified by experts based on several pathological criteria. To reduce potential errors by pathologists and expedite the result acquisition process, more precise outcomes are achieved through automated classification methods.

2. Materials and Methods

This study evaluated the histopathological effects of cisplatin and exosome treatments on ovarian tissues using advanced image processing and machine learning methods. First, histopathological images of ovarian tissues were obtained, with follicles selected and subjected to a patching process. Ground-truth data were established for the selected follicles, followed by image segmentation. After segmentation, Local Binary Pattern (LBP)-based texture features were extracted from the RGB channels. These features were grouped into four classes to analyze the effects of cisplatin and exosome treatments. The extracted features were classified using machine learning algorithms such as Artificial Neural Networks

(ANNs), k-nearest neighbors (KNN), Support Vector Machines (SVMs), and decision tree (DT). The flow chart of the proposed study is shown in Figure 1.

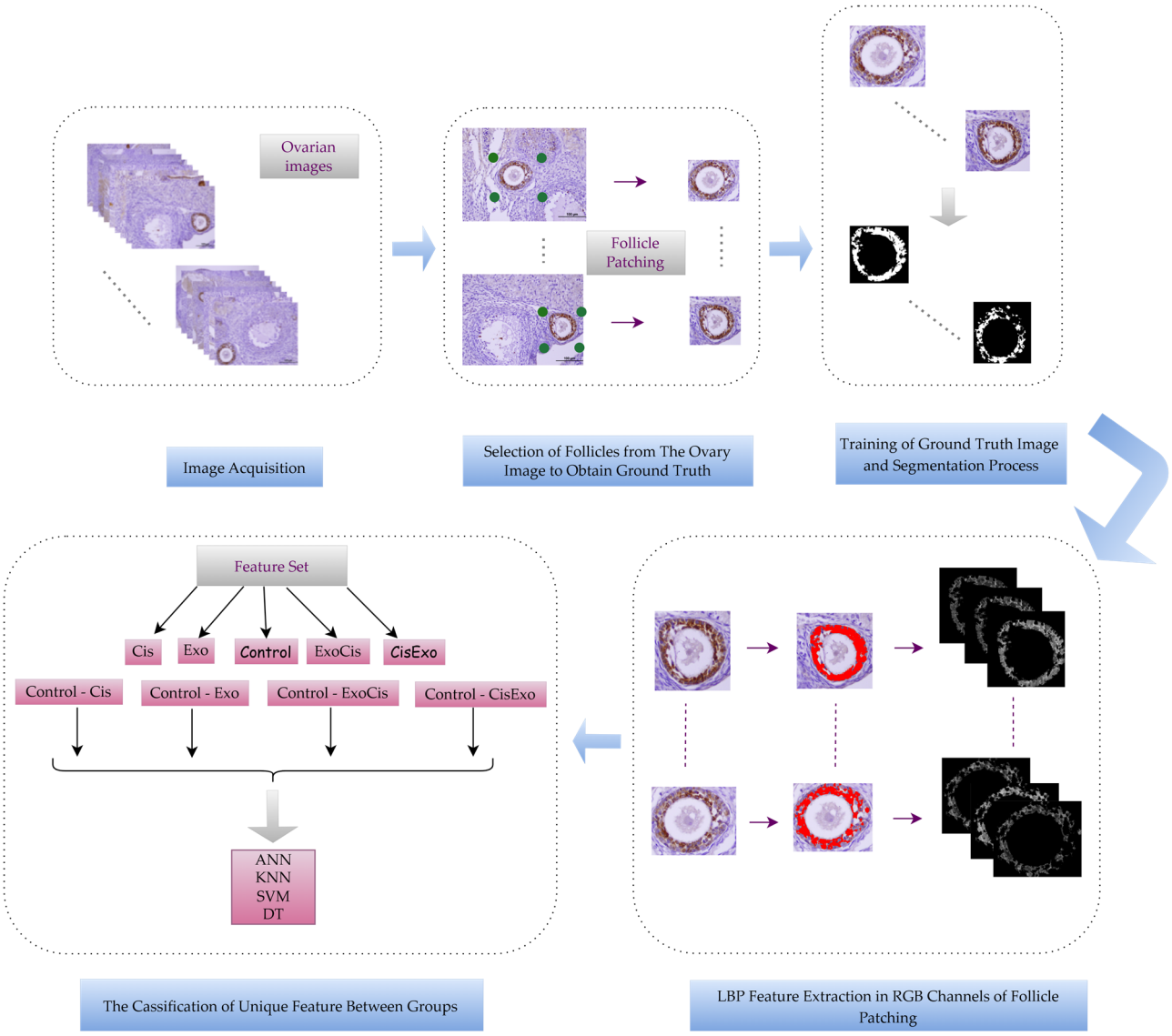

Figure 1. The flow chart of the proposed study.

2.1. Description of Histopathology Dataset

2.1.1. Animals and Experimental Protocol

The experimental protocol adhered to institutional guidelines for animal experiments and was approved by the Ethics Committee of Erciyes University Animal Production and Research Center. The study involved 50 healthy adult female Wistar albino rats (aged 2–3 months, weighing 200–250 g) obtained from the Experimental and Clinical Research Center of Erciyes University. The animals were housed in plastic cages under controlled conditions (21 ± 3 °C, 12 h light/12 h dark cycle) in a well-ventilated room. Food and water were provided ad libitum. The animals were randomly divided into five groups of 10 rats each. The Control group received no treatment. Cisplatin-group rats received two single doses of intraperitoneal cisplatin (5 mg/kg, ip) once a week; Exosome-group rats were administered 100 µL of saline containing 10 × 106 mesenchymal stem cell-derived exosomes intravenously (iv) via the tail vein; Exosome + Cisplatin-group rats were pre-treated with exosomes (10 × 106 iv) 30 min prior to cisplatin injection (5 mg/kg/week, ip); Cisplatin + Exosome-group rats received cisplatin injection (5 mg/kg/week, ip) followed

by mesenchymal stem cell-derived exosomes (10 × 106 iv) 30 min later. In the remainder of the study, Exo + Cis will be referred to as ExoCis, and Cis + Exo will be referred to as CisExo. All experimental procedures were performed at the same time each day. The second round of administration was performed one week after the first, using identical injections and procedures for ip and/or iv administration. Exosomes were isolated from mesenchymal stem cells and prepared based on the Good Manufacturing Practices (GMP) standards in the laboratories of Erciyes University.

2.1.2. Histological Examination and Immunohistochemistry

Five days after the second administration, the rats were sacrificed under high-dose xylazine (Alfazyne; Alfasan International BV, Woerden, The Netherlands) and ketamine (Ketalar; Eczacıbaşı Pharmaceutical Industry and Trade Inc., Lüleburgaz, Turkey) anesthesia; ovarian tissues were dissected and fixed in 10% neutral formaldehyde for two weeks. The tissues were then washed in 70% alcohol, dehydrated in a graded ethanol series up to 100%, cleared in xylene, and processed through molten paraffin (melting point = 60 °C) before being embedded in paraffin blocks. Sections of 5 μm thickness were obtained using a rotary microtome. The primary antibody used was goat polyclonal anti-AMH antibody (sc-6886; Santa Cruz Biotechnology Inc., Dallas, TX, USA), diluted 1:50. The sections were incubated for 15 min with a biotinylated secondary antibody. After washing with PBS, the sections were treated with 3,3′-diaminobenzidine tetrachloride (DAB) as a chromogen for 3–5 min at room temperature. After rinsing with deionized water, the nuclei were counterstained with hematoxylin and mounted using Entellan. The sections were examined under a light microscope (Olympus BX51, Tokyo, Japan).

2.2. Image Acquisition

Histopathological images obtained from the Experimental and Clinical Research Center of Erciyes University were analyzed using a k-nearest neighbor (k-NN) model. The model was employed to define regions of interest (ROIs), focusing specifically on follicles containing oocytes. Ground-truth images manually annotated by experts were used to guide the k-NN model in segmenting the images. The model identified four reference points to delineate the boundaries of specific regions within the images, ensuring accurate segmentation of follicular regions containing oocytes. Regions identified by the model were cropped from the original images to create new ones for detailed analysis. The images were acquired with an initial resolution of 432 dpi. Following preprocessing, the resolution was preserved to retain the quality of the critical features for analysis.

In the newly generated images, we have 36 samples from the Cisplatin (Cis) class, 23 samples from the Exosome (Exo) class, 8 samples from the Cisplatin+Exo (CisExo) class, 10 samples from the Exosome+Cisplatin (ExoCis) class, and 14 samples from the Control class. The distribution of images across these groups was imbalanced. For the classification model to produce accurate and reliable results, each class (group) must be adequately represented. To address this imbalance and prevent biased learning—where the model might prioritize majority classes while underrepresenting minority classes—the ADASYN (Adaptive Synthetic Sampling) method was employed [31].

ADASYN is specifically designed to address this issue by improving classification performance when minority classes are underrepresented. It increases the number of minority-class samples by generating new synthetic examples that are similar but not identical to the existing data. The process involves the following:

- Weighting of samples.
  - The neighbors of each minority class sample are identified.
- More synthetic data are generated for minority-class samples in less-represented regions.

- Synthetic data generation.
- For each minority-class sample, synthetic data points are created through linear interpolation between the sample and its k-nearest neighbors.
- Adaptive approach.
    - Depending on the density of minority class samples, different numbers of synthetic data points are generated. Less-dense areas receive more synthetic data.

This method generates synthetic samples to strengthen the representation of minority classes, such as CisExo (8) and ExoCis (10), ensuring balanced learning across all groups. As a result, the classification model is expected to produce more balanced and accurate results.

2.3. Training Process of the Obtained Images

The newly obtained images were used to train a k-NN (k-nearest neighbors) classifier [32]. During the training process, specific points around the follicular region (brown, white, and purple areas) were labeled to develop a model based on these annotations. The images were scanned to gather the necessary data for training. The k-NN algorithm was used to train the model, with the parameter k set to 3 based on experimental evaluation. This value was chosen as it provided the best balance between model accuracy and computational efficiency during preliminary testing (k = 3) [33]. Manual labeling of specific regions was essential for developing the machine learning model. Once the classes were defined, the model automatically applied them to all images.

2.4. Feature Extraction

Local Binary Pattern—LBP

The LBP operator is a method used to describe the texture of an image by evaluating the relationships between a pixel and its neighbors [34]. The process involves the following steps:

- Window selection: For each pixel, a specific neighborhood (usually a 3 × 3 window) is selected around it.
- Comparison: The intensity of the central pixel is compared to the intensities of the neighboring pixels. If a neighboring pixel has an intensity greater than or equal to the central pixel, it is marked as 1; if it is smaller, it is marked as 0.
- Binary encoding: The obtained 0s and 1s are arranged in a specific order to form a binary number.
- Pattern assignment: The binary number is assigned as the value of the central pixel, thus generating the LBP codes.
- Histogram creation: After extracting the LBP codes for all pixels, a histogram of these codes is created to obtain texture features.

In general, $LBP_{P,R}$ can be defined with three different circular neighborhoods where P represents the number of neighbors and R represents the sampling radius. The LBP operators we used are shown in Figure 2 [34,35].

$$LBP_{P,R}(x_c) = \sum_{p=0}^{P-1} u(x_p - x_c)2^p \quad (1)$$

$$u(y) = \{1,\ y\ \geq 0 \quad 0, y < 0\}$$

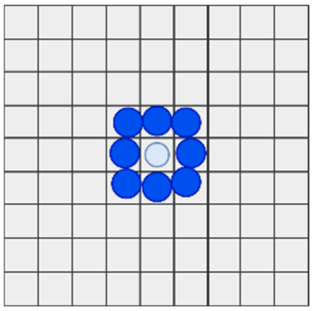

Figure 2. Used circular $LBP_{P,R}$ operators.

Here, *Xc* represents the generated center pixel, *Xp* represents the neighbors of *Xc*, *R* is the distance from the center pixel to the neighbors, and *P* is the number of neighbors involved in the processing.

In this analysis, 3 × 3 windows were chosen as they effectively capture local texture information while being computationally efficient. This window size allows each central pixel to be compared with its eight neighboring pixels ($LBP_{8,1}$), making it possible to capture the fine details of the local texture. In this study, for all images, a total of 177 features were obtained from the RGB (Red, Green, Blue) channels, with 59 LBP features extracted from each channel. When selecting the most important features from these, Lasso (Least Absolute Shrinkage and Selection Operator) regression [36] was used. Lasso regression is a popular regression method used to identify important features and eliminate unnecessary ones in high-dimensional datasets. In cases where there are many features, it improves the model's performance and reduces overfitting by shrinking some regression coefficients to zero, ensuring that only the most important features remain in the model. Figure 3 shows how LBP operates on a sample image.

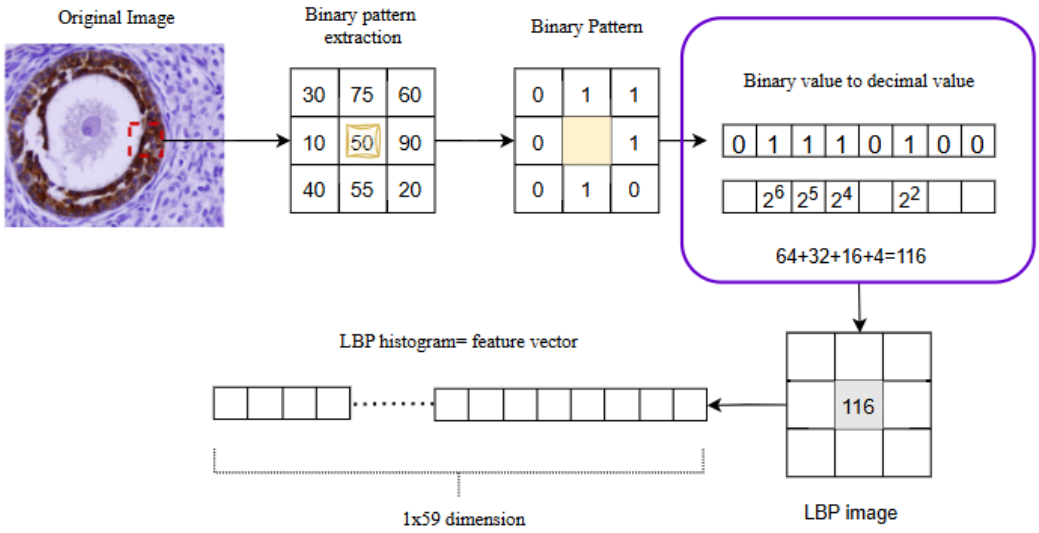

Figure 3. LBP operates on a sample image.

Mathematical interpretation of Lasso regression: Lasso regression is a method used to select important features from a dataset and eliminate unnecessary ones. This method prevents overfitting by shrinking some regression coefficients to zero, thus retaining only the most important features. The Lasso regression problem is explained by the formula given in Equation (2).

$$\sum_{i=1}^{n}\left(y_i - \sum_{j=1}^{p}\beta_j x_{ij}\right)^2 + \lambda\sum_{j=1}^{p}|\beta_j| \quad (2)$$

- y_i: target variable;
- x_{ij}: input features;
- β_j: regression coefficients;
- λ: the lambda parameter.

In this study, the lambda parameter was experimentally set to 0.0005 for the Cis, Exo, ExoCis, CisExo, and Control groups. As the lambda value increases, more coefficients converge to zero, and thus fewer features remain in the model.

2.5. Classification Methods

2.5.1. Support Vector Machines

Support Vector Machines (SVMs) are widely used machine learning methods in data-driven research fields. They aim to find the optimal hyperplane that separates different classes in classification problems [37–40]. SVM maximizes the margin between support vectors of different classes, ensuring optimal class separation. In non-linear datasets, SVMs cannot create a linear hyperplane. Therefore, kernel functions are used to transform the data into a higher dimensional space where linear separation can be performed [41].

2.5.2. K-Nearest Neighbors (KNN)

K-nearest neighbors (k-NN) is a non-parametric classification method that assigns a class to the data based on the similarity to other data points in the training set, by calculating the distance to the k-nearest data points [42–44]. The k-parameter in this method determines how many neighbors the data will be compared to. The classification accuracy can be improved by experimentally determining the optimal value of k.

2.5.3. Artificial Neural Networks (ANNs)

Artificial Neural Networks (ANNs) are computational systems made up of simple processing units (artificial neurons) that mimic the functions of the human brain [42,45,46]. ANNs consist of inputs, weights, summation functions, activation functions, and outputs. The goal of a neural network is to minimize the error between the outputs and the actual values by adjusting the weights optimally. To achieve this, the weights are continuously updated until the error falls below a threshold.

2.5.4. Decision Tree

Decision trees are logical models used to predict the value of a dependent variable based on the values of independent variables [47–49]. A decision tree starts at the root and branches out into leaves. Each feature (attribute) in the data represents the nodes of the tree, while the leaves represent the class labels. The paths between nodes create the classification rules [50]. Decision trees are frequently preferred due to their easy-to-interpret structure

Hyperparameter Optimization

In this study, Bayesian Optimization was applied for hyperparameter optimization of the machine learning methods used. Bayesian Optimization is an effective approach for increasing model accuracy and minimizing the trial-and-error process during hyperparameter selection.

2.6. Performance Metrics

To evaluate the prediction performance of classification models, metrics such as the confusion matrix, precision, recall, F1 score, and accuracy are used. The confusion matrix is one of the intuitive metrics used to determine the accuracy of a model [51]. It is a table produced by comparing the predicted values with the actual data expressing whether the model produces correct results using four metrics. These four metrics consist of True

Positive (TP), True Negative (TN), False Positive (FP), and False Negative (FN) values. The confusion matrix is shown in Figure 4.

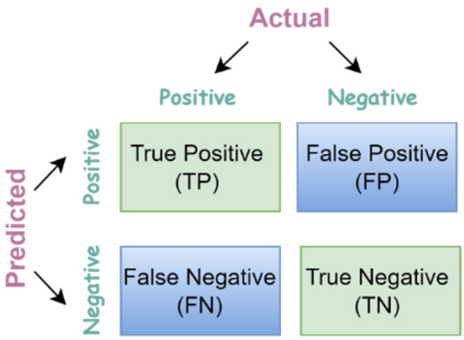

Figure 4. Confusion matrix.

The values obtained from the confusion matrix are as follows:

- Accuracy indicates the proportion of correct predictions for the obtained data, as shown in Equation (3) [52]:

$$\text{Accuracy} = \frac{TP + TN}{TP + FP + TN + FN} \tag{3}$$

- Sensitivity (also known as recall) is a metric that shows how many of the cases that should have been predicted as positive were actually predicted as positive [52]. It is calculated as shown in Equation (4):

$$\text{Sensitivity} = \frac{TP}{TP + FN} \tag{4}$$

- Precision indicates how many of the values predicted as positive are actually positive [52]. It is calculated as shown in Equation (5):

$$\text{Precision} = \frac{TP}{TP + FP} \tag{5}$$

- F1 score is the most standard way to represent the balance between precision and sensitivity in a single performance measure. The F1 score is obtained by calculating the harmonic mean of these metrics instead of their arithmetic mean, as shown in Equation (6) [52]:

$$\text{F1 score} = \frac{2 * \text{Precision} * \text{Sensitivity}}{\text{Precision} + \text{Sensitivity}} \tag{6}$$

- Specificity is a measure of how well the classifier predicts the True Negative values. The formula is shown in Equation (7) [52]:

$$\text{Specifity} = \frac{TN}{TN + FP} \tag{7}$$

3. Results

The proposed study aims to analyze the effects of cisplatin (a chemotherapy drug) [53] and exosomes derived from mesenchymal stem cells, which have a reparative effect [54], on the female ovaries of cancer patients. In this study, we have five groups: Cis (cisplatin-treated groups), Exo (exosome-treated groups), ExoCis (groups treated with exosome followed by cisplatin), CisExo (groups treated with cisplatin followed by exosome) and Control (healthy groups).

According to the information obtained from pathology experts [55], it is known that the exosome treatment group for cancer patients has a reparative effect [54] and its results

are close to the Control group. A noticeable difference is observed between the Control group and the cisplatin-treated cancer patients. Based on this information provided by experts, to present more definitive results regarding the comparisons between groups, the results were analyzed by classifying them using machine learning methods such as ANN, SVM, KNN, and DT.

The classification was performed by creating groups between the Control group and the Cisplatin and Exosome groups, as shown in Figure 5.

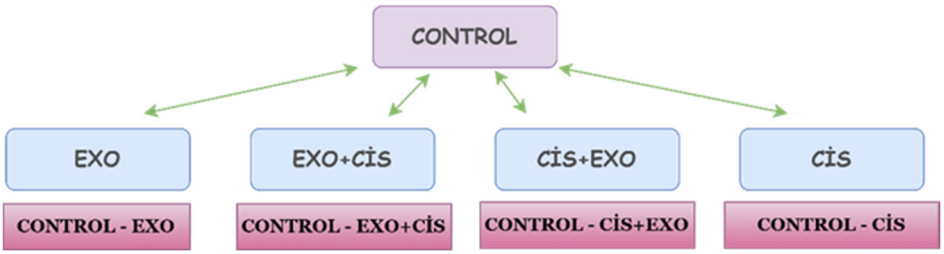

Figure 5. Classification groups.

During the study, 59 LBP features were extracted from each of the RGB (Red, Green, Blue) channels for the images in each group, resulting in a total of 177 features per image. Despite the complexity and limited distinctiveness of other features, LBP was chosen for this study due to its ability to represent tissue differences quickly, efficiently, and with high accuracy [56]. The distribution of the mean LBP features for each group is illustrated in Figure 6 using a violin plot. Lower LBP values indicate a more homogeneous tissue structure, whereas higher values reflect increased heterogeneity. In the graph, the CisExo group exhibits a narrow distribution, indicating that its features are concentrated within a specific range and show low variance. This suggests that the CisExo group has a more homogeneous texture. In contrast, the ExoCis group displays a broader distribution compared to the other groups, with higher intensity at the extremes, indicating greater variability in feature values. This broad distribution suggests that the ExoCis group may possess a more heterogeneous texture. The Control group, on the other hand, exhibits a moderately wide distribution, with most features concentrated around a central value and less spread toward the extremes. This indicates that the Control group has a moderately homogeneous structure. In conclusion, the LBP features reveal that the CisExo group has the most homogeneous structure, while the ExoCis group shows the highest heterogeneity and variability. The observation that the ExoCis group is more heterogeneous than the CisExo group but closer to the Control group suggests fewer pronounced pathological changes. These findings indicate that the ExoCis group may have undergone a better recovery process compared to the CisExo group.

The extracted LBP features were analyzed using statistical methods. However, due to the large number of features (177 in total), the results were not included in the manuscript but were provided as a Supplementary File. A normality test was performed for all features; however, as none of the features followed a normal distribution, the Kruskal–Wallis test was applied to all of them. For features that showed significant differences among groups, a post hoc analysis (Dunn test) was performed to identify which groups (Cis, Exo, CisExo, ExoCis, and Control) differed significantly. As a result, 51 features were found to exhibit significant differences, and post hoc analysis revealed significant differences specifically between the CisExo-Cis and CisExo-Exo groups. Please refer to the Supplementary File for detailed statistical test results (p-values). The statistical test analyses were performed using the R statistical software (R-4.4.2 version).

Unique features for each feature set were selected from the extracted features. Subsequently, the classification results of these features between the Control and Cisplatin

groups were evaluated. As shown in Table 1, the DT classification achieved an accuracy of 73% ± 0.06 and an F-score of 75% ± 0.03 for the Control and Cisplatin groups. In contrast, the KNN, ANN, and SVM methods achieved accuracy values close to 91.33%.

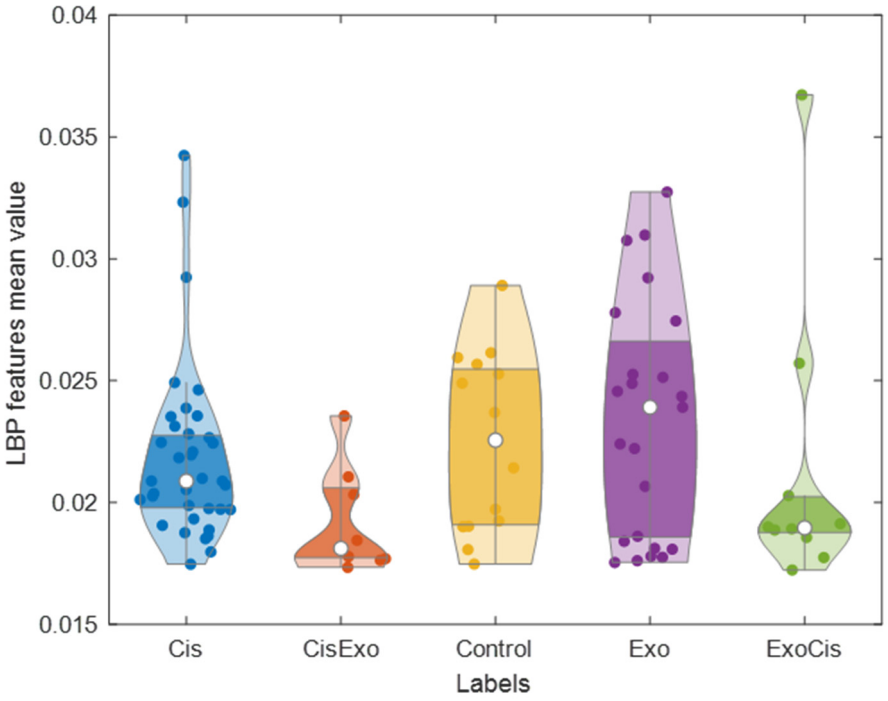

Figure 6. A violin graph displaying the mean of 177 features.

Table 1. Performance metrics for classification between Control and Cisplatin groups.

	Accuracy	CorrecRate	Sensitivity	Specificity	Precision	NPV	F-Score
DT	0.73 ± 0.06	0.75 ± 0.02	0.74 ± 0.05	0.76 ± 0.04	0.77 ± 0.03	0.73 ± 0.03	0.75 ± 0.03
KNN	0.92 ± 0.02	0.92 ± 0.02	0.90 ± 0.02	0.95 ± 0.03	0.95 ± 0.03	0.90 ± 0.01	0.92 ± 0.02
SVM	0.90 ± 0.02	0.87 ± 0.01	0.81 ± 0.02	0.93 ± 0.04	0.93 ± 0.04	0.82 ± 0.01	0.86 ± 0.01
ANN	0.92 ± 0.05	0.86 ± 0.05	0.81 ± 0.04	0.92 ± 0.1	0.92 ± 0.09	0.82 ± 0.04	0.86 ± 0.05

The classification results between the Control and Exo groups are presented in Table 2. The SVM classification achieved an accuracy of 59% ± 0.07 and an F-score of 57% ± 0.08. Meanwhile, the DT, KNN, and ANN methods achieved approximately 68.33% accuracy, with F-scores of 75% ± 0.03, 65% ± 0.04, and 60% ± 0.02, respectively.

Table 2. Performance metrics for classification between Control and Exo groups.

	Accuracy	CorrecRate	Sensitivity	Specificity	Precision	NPV	F-Score
DT	0.67 ± 0.04	0.73 ± 0.03	0.78 ± 0.03	0.67 ± 0.05	0.72 ± 0.03	0.74 ± 0.04	0.75 ± 0.03
KNN	0.70 ± 0.04	0.67 ± 0.01	0.60 ± 0.09	0.75 ± 0.09	0.73 ± 0.04	0.64 ± 0.03	0.65 ± 0.04
SVM	0.59 ± 0.07	0.57 ± 0.08	0.55 ± 0.07	0.60 ± 0.11	0.60 ± 0.09	0.55 ± 0.08	0.57 ± 0.08
ANN	0.68 ± 0.05	0.65 ± 0.03	0.51 ± 0.04	0.79 ± 0.08	0.74 ±0.06	0.60 ± 0.01	0.60 ± 0.02

The results of the Control and CisExo groups are analyzed in Table 3. After analyzing the KNN classification results, an F-score of 89% ± 0.04 and an accuracy of 90% ± 0.03 were achieved. In the SVM results, an accuracy of 86% ± 0.07 and an F-score of 88% ± 0.06 were obtained. For the DT classification, an accuracy of 76% ± 0.12 and an F-score of 77% ± 0.08

were recorded, while in ANN, an accuracy of 88% ± 0.05 and an F-score of 89% ± 0.05 were achieved.

Table 3. Performance metrics for classification between Control and CisExo groups.

	Accuracy	CorrecRate	Sensitivity	Specificity	Precision	NPV	F-Score
DT	0.76 ± 0.12	0.75 ± 0.08	0.78 ± 0.11	0.73 ± 0.06	0.76 ± 0.06	0.75 ± 0.11	0.77 ± 0.08
KNN	0.90 ± 0.03	0.89 ± 0.04	0.85 ± 0.03	0.93 ± 0.05	0.93 ± 0.05	0.84 ± 0.04	0.89 ± 0.04
SVM	0.86 ± 0.07	0.87 ± 0.06	0.90 ± 0.06	0.84 ± 0.08	0.87 ± 0.06	0.88 ± 0.06	0.88 ± 0.06
ANN	0.88 ± 0.05	0.87 ± 0.06	0.91 ± 0.07	0.83 ± 0.11	0.86 ± 0.07	0.90 ± 0.08	0.89 ± 0.05

The results for the Control and ExoCis groups are shown in Table 4. According to the evaluation results, the accuracy for SVM, ANN, and KNN classification is approximately 74.66%, while the DT classification yields an accuracy of 61% ± 0.02.

Table 4. Performance metrics for classification between Control and ExoCis groups.

	Accuracy	CorrecRate	Sensitivity	Specificity	Precision	NPV	F-Score
DT	0.61 ± 0.02	0.70 ± 0.05	0.62 ± 0.00	0.79 ± 0.10	0.74 ± 0.09	0.69 ± 0.03	0.67 ± 0.04
KNN	0.75 ± 0.04	0.70 ± 0.06	0.82 ± 0.07	0.60 ± 0.13	0.66 ± 0.07	0.78 ± 0.06	0.73 ± 0.04
SVM	0.75 ± 0.05	0.75 ± 0.06	0.89 ± 0.04	0.61 ± 0.14	0.69 ± 0.09	0.86 ± 0.04	0.78 ± 0.04
ANN	0.74 ± 0.06	0.68 ± 0.02	0.71 ± 0.08	0.66 ± 0.09	0.66 ± 0.04	0.71 ± 0.03	0.68 ± 0.03

The distribution of accuracy values obtained for the Control–Cis, Control–CisExo, Control–Exo, and Control–ExoCis groups using four different classification algorithms (DT, KNN, SVM, ANN) across five trials is illustrated in Figure 7.

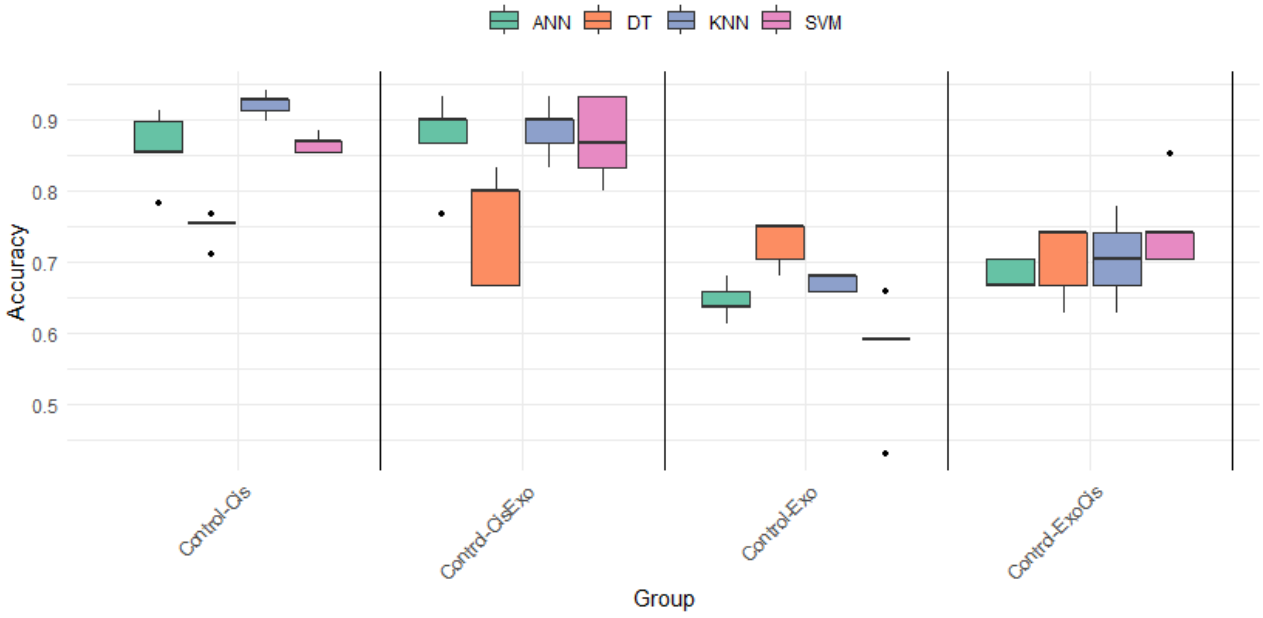

Figure 7. Accuracy results of five different groups' classification performance.

The performance of each classification algorithm varies among the different groups. For instance, in the Control–Cis group, the KNN and DT algorithms exhibited higher accuracy rates compared to other models. However, SVM and ANN models demonstrated a wider range of accuracy values, occasionally yielding lower accuracy scores. This suggests that these models may be more affected by variances within this group.

In the Control–CisExo group, the DT model achieved the highest accuracy. Similarly, the KNN and ANN models also produced high accuracy rates, while the SVM model's accuracy was generally lower. This indicates that the SVM model performed less effectively for this group.

In the Control–Exo group, there was a noticeable difference between the DT and ANN models. The DT model generally performed better, whereas the KNN model yielded lower accuracy compared to other models. This group highlights the DT model as the standout performer, providing higher accuracy rates overall.

For the Control–ExoCis group, the ANN and SVM models achieved higher accuracy rates, while the accuracy values for the KNN model were spread across a wider range. The DT model demonstrated lower accuracy in the Control–ExoCis group.

4. Discussion

This study aimed to identify the damage caused by cisplatin, a chemotherapeutic agent administered to cancer patients, on female ovarian tissue and to analyze the restorative effects of exosomes derived from mesenchymal stem cells. The classification results for Cis, Exo, Control, CisExo, and ExoCis groups were evaluated.

Images from the female reproductive system, particularly follicular images containing oocytes, obtained from the pathology laboratory were included in the analysis. To define the region's boundaries in the images, a model based on artificial intelligence was used to select four reference points. Oocyte-containing follicles were cropped from the images within the specified coordinates, generating new images for detailed analysis.

A total of 177 features were extracted per image, including 59 LBP features from each RGB channel. A k-NN classifier was used [32]. Specific points around the follicle (brown, white, and purple regions) were labeled. This trained model was then applied to all images to generate enhanced, trained versions of the images.

To identify the most significant features, Lasso regression was applied with an experimentally determined lambda value [36]. The selected unique features for each group were classified using ANN, KNN, SVM, and DT models. The selected distinctive features enhanced classification precision.

Due to the restorative effects of the Exosome group, experts hypothesized its similarity to the Control group. Upon examining the accuracy values of classification models for the Control–Exo group in Table 2, DT achieved 67% $\pm$ 0.04, KNN achieved 70% $\pm$ 0.04, SVM achieved 59% $\pm$ 0.07, and ANN achieved 68% $\pm$ 0.05. The classification performance of the models was lower for the Control–Exo group compared to the Control–Cisplatin group, likely due to the similarity of features selected for the Control and Exo groups. Furthermore, the violin plot shown in Figure 6 confirms that the Control group and the Exo group are similar in terms of features.

For the Control–Cisplatin group, a high classification performance was anticipated due to the selection of distinctive features. As shown in Table 1, the results for KNN, SVM, and ANN were 92% $\pm$ 0.02, 90% $\pm$ 0.02, and 92% $\pm$ 0.05 accuracy, respectively. The significant differences in the features between the Control and Cisplatin groups enabled the classification models to distinguish these groups with approximately 91.33% accuracy.

The classification results for the Control and Exo-Cis groups (Table 4) revealed an accuracy of 61% $\pm$ 0.02 for the DT model, while KNN, ANN, and SVM achieved approximately 74.66% accuracy. Despite expectations that the Control–ExoCis group would yield results similar to the Control–Cis group, it was observed that administering exosomes before cisplatin had a modest restorative effect, reducing the impact of cisplatin compared to the Control–Cis group.

Analysis of the Control and Cis-Exo groups (Table 3) revealed that the exosome administered after cisplatin was expected to have a restorative effect, leading to similarities between the Control group and Cis-Exo group's distinctive features. Contrary to expectations, DT achieved 76% $\pm$ 0.12 accuracy, whereas the other models yielded approximately 87% accuracy. These findings suggest that exosomes administered after cisplatin did not effectively restore the damage caused by cisplatin.

In the classification of Control and Cis groups, the KNN algorithm outperformed others with an accuracy of 92% and an F-score of 92%. Similarly, ANN and SVM algorithms demonstrated strong performances, achieving over 90% accuracy. For the Exo and Control groups, ANN provided balanced results with an accuracy of 68% and an F-score of 60%. Particularly in the CisExo group, the high accuracy and F-score values obtained by ANN and KNN algorithms indicated that the features of this group were more effectively learned.

According to the boxplot results in Figure 1, DT and ANN models displayed narrower accuracy ranges and lower standard deviations, reflecting more consistent and stable performance. These models achieved similar accuracy levels across different groups, demonstrating less variability. On the other hand, KNN and SVM models exhibited broader accuracy ranges and higher standard deviations, indicating more variable performance. SVM, in particular, showed low accuracy in some groups, resulting in more pronounced fluctuations and higher standard deviation. Overall DT and ANN provided more consistent results, while KNN and SVM showed greater variability.

The analyses suggest that exosome administration may be an effective method to mitigate the side effects of cisplatin on ovarian tissue in female cancer patients. Additionally, this study highlights the potential of exosome-based therapeutic approaches to reduce chemotherapy side effects. The high homogeneity and classification success observed in the CisExo group support the notion that exosome application can alleviate cisplatin-induced damage. This finding is significant for developing strategies to minimize cisplatin's side effects and preserve reproductive health post-cancer treatment.

The analysis of LBP features was conducted using statistical methods, resulting in a total of 177 features. Since none of the features followed a normal distribution according to the normality test, the Kruskal–Wallis test [57,58] was applied. For features that showed significant differences, a post hoc Dunn test [57] was performed, identifying 51 features with significant differences. Notably, significant differences were observed between the CisExo-Cis and CisExo-Exo groups. When visualized based on p-values [57] for the significant features, feature 114 demonstrated better performance compared to the others.

To further evaluate classification performance and provide a comparative perspective, we also applied a deep learning-based approach using AlexNet. Below, we summarize its methodology and findings.

A five-fold cross-validation strategy was applied, with training and test datasets randomly split for each fold. Transfer learning was employed by fine-tuning AlexNet's pre-trained network, where the final layers were modified to match the dataset. The training process used the Adam optimizer with a learning rate of 0.0001, a mini-batch size of 16, and 12 epochs. Classification performance was evaluated using precision, recall, specificity, accuracy, and F1-score metrics. The results revealed that the highest classification accuracy was achieved in the Control vs. Cisplatin group, consistent with the distinct textural alterations caused by cisplatin. The lowest accuracy was observed in the Control vs. Exosome group, supporting the finding that exosome-treated tissues closely resemble the Control group in texture. Furthermore, the Exosome + Cis group showed lower classification accuracy compared to Cis + Exosome, reinforcing the significance of treatment sequence on tissue recovery. While AlexNet-based deep learning provided robust classification performance, its inability to elucidate specific histopathological feature

changes limits its interpretability. Therefore, LBP-based feature extraction and machine learning approaches remain more suitable for understanding the mechanistic effects of cisplatin and exosome treatments on ovarian tissue structure.

For the first time in the literature, this study analyzed the effects of cisplatin and exosomes on female ovarian tissues using histopathological images with LBP-based feature extraction and machine learning classification methods. The multiclass framework, including different combinations of cisplatin and exosome treatments, provided a detailed examination of pre- and post-treatment conditions. This study introduces a novel approach for clinical and biomedical research. By comparing the performance of various machine learning algorithms, the effects of cisplatin and exosomes were analyzed more precisely.

5. Conclusions

In conclusion, previous studies highlight that exosomes possess advantages such as high biocompatibility and long-term circulation, making them an ideal candidate for therapeutic effects [59,60]. In light of this information, this study demonstrates for the first time that exosome pre- and post-treatment applications reduce cisplatin-induced ovarian damage in rats, through feature extraction using the LBP method and classification of the obtained results using machine learning techniques (Tables 1–4). The findings derived from LBP-based feature extraction reveal significant differences between the groups and indicate that the reparative effect of exosomes is reflected both at the tissue and classification metric levels. According to our study's findings, exosome treatment in cancer patients has been supported by classification results showing that it can improve ovarian follicle and oocyte quality by exhibiting anti-inflammatory and anti-apoptotic effects. The characteristics of the Exosome group, which showed similar results to the Control groups, and some features that could not be classified, leading to lower values compared to other groups, are shown in Table 2. The data from this study also quantitatively demonstrate the therapeutic potential of exosomes. Additionally, in line with predictions by expert pathologists, the increase in AMH levels, and the decrease in cytokine production, exosome treatment prior to cisplatin administration resulted in more morphologically normal follicles and less apoptosis compared to the Cis + Exo treatment group [61].

The results obtained point to the potential of the novel methods we used for the first time in this field to provide an innovative contribution to pathological findings in the literature.

Supplementary Materials: The supporting information can be downloaded at https://www.mdpi.com/article/10.3390/app15041984/s1. Table S1: Significant features as a result of statistical analysis.

Author Contributions: Methodology, T.Ş. and F.L.; data acquisition, A.Y., Z.B.G., Ö.C.M., Y.Ö. and G.Ö.Ö.; analysis, F.L., T.Ş. and Ç.G.A.; validation, F.L. and T.Ş.; writing—original draft preparation, T.Ş.; writing—review and editing, F.L. All authors have read and agreed to the published version of the manuscript.

Funding: This study was supported by the Erciyes University Scientific Research Projects Unit under the project number TSG-2021-11527. The authors sincerely thank the Erciyes University Scientific Research Projects Unit for their financial support and encouragement throughout this research.

Institutional Review Board Statement: The animal study protocol was approved by the Ethics Committee of Erciyes University Animal Production and Research Center (protocol code: 21/249) for studies involving animals.

Informed Consent Statement: Not applicable.

Data Availability Statement: The data presented in this study are available on request from the corresponding author.

Conflicts of Interest: The authors declare no conflicts of interest.

References

1. Baykara, O. Kanser Tedavisinde Güncel Yaklaşimlar. *Balıkesir Sağlık Bilim. Derg.* **2016**, *5*, 154–165.
2. Türk, G. Kemoterapötiklerin erkek üreme sistemi üzerindeki yan etkileri ve koruyucu stratejiler. *Marmara Pharm. J.* **2013**, *17*, 73–92. [CrossRef]
3. Chapman, R.M. Effect of cytotoxic therapy on sexuality and gonadal function. *Semin. Oncol.* **1982**, *9*, 84–94.
4. Collichio, F.; Pandya, K. Amenorrhea following chemotherapy for breast cancer: Effect on disease-free survival. *Oncology* **1994**, *8*, 45–52. [PubMed]
5. Chasle, S.; How, C.C. The effect of cytotoxic chemotherapy on female fertility. *Eur. J. Oncol. Nurs.* **2003**, *7*, 91–98. [CrossRef]
6. Henke, Y.C.; Wujcik, D.; Holmes, G.B. *Cancer Nursing: Principles and Practice*; Jones & Bartlett Learning: Burlington, MA, USA, 2016.
7. Partridge, A.H.; Garber, J.E. Long-term outcomes of children exposed to antineoplastic agents in utero. *Semin. Oncol.* **2000**, *27*, 712–726.
8. Nonomura, M.; Okada, K.; Hida, S.; Yoshida, O. Does a gonadotropin-releasing hormone analogue prevent cisplatin-induced spermatogenic impairment? An experimental study in the mouse. *Urol. Res.* **1991**, *19*, 135–140. [CrossRef] [PubMed]
9. Dasari, S.; Tchounwou, P.B. Cisplatin in cancer therapy: Molecular mechanisms of action. *Eur. J. Pharmacol.* **2014**, *740*, 364–378. [CrossRef]
10. Weijl, N.; Hopman, G.; Wipkink-Bakker, A.; Lentjes, E.; Berger, H.; Cleton, F.; Osanto, S. Cisplatin combination chemotherapy induces a fall in plasma antioxidants of cancer patients. *Ann. Oncol.* **1998**, *9*, 1331–1337. [CrossRef]
11. Olas, B.; Wachowicz, B. Resveratrol reduces oxidative stress induced by platinum compounds in blood platelets. *Gen. Physiol. Biophys.* **2004**, *23*, 315–326.
12. Sonmezer, M.; Oktay, K. Fertility preservation in female patients. *Hum. Reprod. Update* **2004**, *10*, 251–266. [CrossRef] [PubMed]
13. Sakamoto, H.; Oohta, M.; Inoue, K.; Fuji, K.; Fukagai, T.; Yoshida, H. Testicular sperm extraction in patients with persistent azoospermia after chemotherapy for testicular germ cell tumor. *Int. J. Urol.* **2007**, *14*, 167–170. [CrossRef]
14. Ding, D.-C.; Chang, Y.-H.; Shyu, W.-C.; Lin, S.-Z. Human umbilical cord mesenchymal stem cells: A new era for stem cell therapy. *Cell Transplant.* **2015**, *24*, 339–347. [CrossRef] [PubMed]
15. Yang, W.; Zhang, J.; Xu, B.; He, Y.; Liu, W.; Li, J.; Zhang, S.; Lin, X.; Su, D.; Wu, T.; et al. HucMSC-derived exosomes mitigate the age-related retardation of fertility in female mice. *Mol. Ther.* **2020**, *28*, 1200–1213. [CrossRef] [PubMed]
16. Mendt, M.; Rezvani, K.; Shpall, E. Mesenchymal stem cell-derived exosomes for clinical use. *Bone Marrow Transplant.* **2019**, *54* (Suppl. S2), 789–792. [CrossRef]
17. Li, B.; Cao, Y.; Sun, M.; Feng, H. Expression, regulation, and function of exosome-derived miRNAs in cancer progression and therapy. *FASEB J.* **2021**, *35*, e21916. [CrossRef] [PubMed]
18. Psaraki, A.; Ntari, L.; Karakostas, C.; Korrou-Karava, D.; Roubelakis, M.G. Extracellular vesicles derived from mesenchymal stem/stromal cells: The regenerative impact in liver diseases. *Hepatology* **2022**, *75*, 1590–1603. [CrossRef]
19. Le Renard, P.-E.; Nimmervoll, B.; Fellner, F.; Oppelt, P. Cisplatin in-vitro activity with co-exposure to MRI. In Proceedings of the 2018 EMF-Med 1st World Conference on Biomedical Applications of Electromagnetic Fields (EMF-Med), IEEE, Split, Croatia, 10–13 September 2018; pp. 1–2.
20. Schwenzer, N.F.; Bantleon, R.; Maurer, B.; Kehlbach, R.; Schraml, C.; Claussen, C.D.; Rodegerdts, E. Detection of DNA double-strand breaks using γh2AX after MRI exposure at 3 Tesla: An In Vitro study. *J. Magn. Reson. Imaging An Off. J. Int. Soc. Magn. Reson. Med.* **2007**, *26*, 1308–1314. [CrossRef]
21. Yu, K.H.; Hu, V.; Wang, F.; Matulonis, U.A.; Mutter, G.L.; Golden, J.A.; Kohane, I.S. Deciphering serous ovarian carcinoma histopathology and platinum response by convolutional neural networks. *BMC Med.* **2020**, *18*, 236. [CrossRef] [PubMed]
22. Bell, D.; Berchuck, A.; Birrer, M.; Chien, J.; Cramer, D.W.; Dao, F.; Dhir, R.; Disaia, P.; Gabra, H.; Glenn, P.; et al. Integrated genomic analyses of ovarian carcinoma. *Nature* **2011**, *474*, 609–615.
23. Krizhevsky, A.; Sutskever, I.; Hinton, G.E. Imagenet Classification with Deep Convolutional Neural Networks. In Proceedings of the Advances in Neural Information Processing Systems 25: 26th Annual Conference on Neural Information Processing Systems 2012, Lake Tahoe, NV, USA, 3–6 December 2012; Volume 25.
24. Szegedy, C.; Liu, W.; Jia, Y.; Sermanet, P.; Reed, S.; Anguelov, D.; Erhan, D.; Vanhoucke, V.; Rabinovich, A. Going Deeper with Convolutions. In Proceedings of the IEEE Conference on Computer Vision and Pattern Recognition, Boston, MA, USA, 7–12 June 2015; pp. 1–9.
25. Simonyan, K.; Zisserman, A. Very Deep Convolutional Networks for Large-Scale Image Recognition. *arXiv* **2014**, arXiv:1409.1556.
26. Lei, R.; Yu, Y.; Li, Q.; Yao, Q.; Wang, J.; Gao, M.; Wu, Z.; Ren, W.; Tan, Y.; Zhang, B.; et al. Deep learning magnetic resonance imaging predicts platinum sensitivity in patients with epithelial ovarian cancer. *Front. Oncol.* **2022**, *12*, 895177. [CrossRef]
27. Ozyurt, R.; Celik, N.; Suleyman, Z.; Cagiran, F.; Kali, Z.; Gurkan, N.; Altindag, F.; Bulut, S.; Sarigul, C.; Dinc, K.; et al. Fertility protective effect of taxifolin in cisplatin-induced ovarian damage. *Eur. Rev. Med. Pharmacol. Sci.* **2022**, *26*, 7195–7203.
28. Sun, W.; Zheng, B.; Qian, W. Automatic feature learning using multichannel ROI based on deep structured algorithms for computerized lung cancer diagnosis. *Comput. Biol. Med.* **2017**, *89*, 530–539. [CrossRef]

29. Patil, S.D.; Deore, P.J.; Patil, V.B. Automated Classification of Ovarian Tumors Using GLCM and Tamura Features with light gbm Classifier. In *Recent Advances in Material, Manufacturing, and Machine Learning*; CRC Press: Boca Raton, FL, USA, 2023; pp. 755–760.
30. Huang, C.-L.; Lian, M.-J.; Wu, Y.-H.; Chen, W.-M.; Chiu, W.-T. Identification of human ovarian adenocarcinoma cells with cisplatin-resistance by feature extraction of gray Level Co-occurrence matrix using optical images. *Diagnostics* **2020**, *10*, 389. [CrossRef] [PubMed]
31. He, H.; Bai, Y.; Garcia, E.A.; Li, S. ADASYN: Adaptive Synthetic Sampling Approach for Imbalanced Learning. In Proceedings of the 2008 IEEE International Joint Conference on Neural Networks (IEEE World Congress on Computational Intelligence), IEEE, Hong Kong, China, 1–8 June 2008; pp. 1322–1328.
32. Kowal, M. Computer-Aided Diagnosis for Breast Tumor Classification Using Microscopic Images of Fine Needle Biopsy. In *Intelligent Systems in Technical and Medical Diagnostics*; Springer: Berlin/Heidelberg, Germany, 2014; pp. 213–224.
33. Surlakar, P.; Araujo, S.; Sundaram, K.M. Comparative Analysis of K-Means and K-Nearest Neighbor Image Segmentation Techniques. In Proceedings of the 2016 IEEE 6th International Conference on Advanced Computing (IACC), IEEE, Bhimavaram, India, 27–28 February 2016; pp. 96–100.
34. Tuncer, T.; Avcı, E. Yerel İkili Örüntü Tabanli Veri Gizleme Algoritmasi: LBP-LSB. *Türkiye Bilişim Vakfı Bilgi. Bilim. Ve Mühendisliği Derg.* **2017**, *10*, 48–53.
35. Yang, B.; Chen, S. A comparative study on local binary pattern (LBP) based face recognition: LBP histogram versus LBP image. *Neurocomputing* **2013**, *120*, 365–379. [CrossRef]
36. Muthukrishnan, R.; Rohini, R. LASSO: A Feature Selection Technique in Predictive Modeling for Machine Learning. In Proceedings of the 2016 IEEE International Conference on Advances in Computer Applications (ICACA), IEEE, Coimbatore, India, 24 October 2016; pp. 18–20.
37. Demirci, M. Destek vektör makineleri ve M5 karar ağacı yöntemleri kullanılarak yağış akış ilişkisinin tahmini. *Dicle Üniversitesi Mühendislik Fakültesi Mühendislik Derg.* **2019**, *10*, 1113–1124.
38. Uslu, O.; Özmen-akyol, S. Türkçe haber metinlerinin makine öğrenmesi yöntemleri kullanılarak sınıflandırılması. *Eskişehir Türk Dünyası Uygul. Ve Araştırma Merk. Bilişim Derg.* **2021**, *2*, 15–20.
39. Korkmaz, S.; Zararsiz, G.; Goksuluk, D. Drug/nondrug classification using support vector machines with various feature selection strategies. *Comput. Methods Programs Biomed.* **2014**, *117*, 51–60. [CrossRef]
40. Torheim, T.; Malinen, E.; Kvaal, K.; Lyng, H.; Indahl, U.G.; Andersen, E.K.F.; Futsaether, C.M. Classification of dynamic contrast enhanced MR images of cervical cancers using texture analysis and support vector machines. *IEEE Trans. Med. Imaging* **2014**, *33*, 1648–1656. [CrossRef]
41. Clement, D.; Agu, E.; Suleiman, M.A.; Obayemi, J.; Adeshina, S.; Soboyejo, W. Multi-class breast cancer histopathological image classification using multi-scale pooled image feature representation (MPIFR) and one-versus-one support vector machines. *Appl. Sci.* **2022**, *13*, 156. [CrossRef]
42. Demir, H.; Erdoğmuş, P.; Kekeçoğlu, M. Destek Vektör Makineleri, YSA, K-Means ve KNN Kullanarak Arı Türlerinin Sınıflandırılması. *Düzce Üniversitesi Bilim Ve Teknol. Derg.* **2018**, *6*, 47–67. [CrossRef]
43. Hatem, M.Q. Skin lesion classification system using a K-nearest neighbor algorithm. *Vis. Comput. Ind. Biomed. Art* **2022**, *5*, 7. [CrossRef]
44. Ajitha, K. SVM vs. KNN for classification of histopathological images of varicose ulcer. *Adv. Eng. An Int. J.* **2020**, *3*, 19–28.
45. Araújo, T.; Aresta, G.; Castro, E.; Rouco, J.; Aguiar, P.; Eloy, C.; Polónia, A.; Campilho, A. Classification of breast cancer histology images using convolutional neural networks. *PLoS ONE* **2017**, *12*, e0177544. [CrossRef] [PubMed]
46. Alhindi, T.J.; Kalra, S.; Ng, K.H.; Afrin, A.; Tizhoosh, H.R. Comparing LBP, HOG and Deep Features for Classification of Histopathology Images. In Proceedings of the 2018 International Joint Conference on Neural Networks (IJCNN), IEEE, Rio de Janeiro, Brazil, 8–13 July 2018; pp. 1–7.
47. Bittencourt, H.R.; Clarke, R.T. Use of Classification and Regression Trees (CART) to Classify Remotely-Sensed Digital Images. In Proceedings of the IGARSS 2003. 2003 IEEE International Geoscience and Remote Sensing Symposium. Proceedings (IEEE Cat. No. 03CH37477), IEEE, Toulouse, France, 21–25 July 2003; pp. 3751–3753.
48. Tabakov, M.; Kozak, P. Segmentation of histopathology HER2/neu images with fuzzy decision tree and Takagi–Sugeno reasoning. *Comput. Biol. Med.* **2014**, *49*, 19–29. [CrossRef]
49. Spanhol, F.A.; Oliveira, L.S.; Petitjean, C.; Heutte, L. A dataset for breast cancer histopathological image classification. *IEEE Trans. Biomed. Eng.* **2015**, *63*, 1455–1462. [CrossRef] [PubMed]
50. Kotsiantis, S.B. Decision trees: A recent overview. *Artif. Intell. Rev.* **2013**, *39*, 261–283. [CrossRef]
51. Cengil, E.; Çınar, A. Göğüs verileri metrikleri üzerinden kanser sınıflandırılması. *Dicle Üniversitesi Mühendislik Fakültesi Mühendislik Derg.* **2020**, *11*, 513–519. [CrossRef]
52. Sevli, O. Göğüs kanseri teşhisinde farklı makine öğrenmesi tekniklerinin performans karşılaştırması. *Avrupa Bilim ve Teknol. Derg.* **2019**, *16*, 176–185. [CrossRef]

53. Florea, A.-M.; Büsselberg, D. Cisplatin as an anti-tumor drug: Cellular mechanisms of activity, drug resistance and induced side effects. *Cancers* **2011**, *3*, 1351–1371. [CrossRef]
54. Ersöz, E.; Can, O.B.; Uzunoğlu, S. Eksozomların kanserdeki rolü. *Celal Bayar Üniversitesi Sağlık Bilim. Enstitüsü Derg.* **2016**, *3*, 144–152.
55. Sun, L.; Li, D.; Song, K.; Wei, J.; Yao, S.; Li, Z.; Su, X.; Ju, X.; Chao, L.; Deng, X.; et al. Exosomes derived from human umbilical cord mesenchymal stem cells protect against cisplatin-induced ovarian granulosa cell stress and apoptosis In Vitro. *Sci. Rep.* **2017**, *7*, 2552. [CrossRef] [PubMed]
56. Reyad, Y.A.; Berbar, M.A.; Hussain, M. Comparison of statistical, LBP, and multi-resolution analysis features for breast mass classification. *J. Med. Syst.* **2014**, *38*, 100. [CrossRef]
57. Nebelung, S.; Brill, N.; Marx, U.; Quack, V.; Tingart, M.; Schmitt, R.; Rath, B.; Jahr, H. Three-dimensional imaging and analysis of human cartilage degeneration using Optical Coherence Tomography. *J. Orthop. Res.* **2015**, *33*, 651–659. [CrossRef] [PubMed]
58. Thomassin-Naggara, I.; Bazot, M.; Daraï, E.; Callard, P.; Thomassin, J.; Cuenod, C.A. Epithelial ovarian tumors: Value of dynamic contrast-enhanced MR imaging and correlation with tumor angiogenesis. *Radiology* **2008**, *248*, 148–159. [CrossRef] [PubMed]
59. Xian, P.; Hei, Y.; Wang, R.; Wang, T.; Yang, J.; Li, J.; Di, Z.; Liu, Z.; Baskys, A.; Liu, W.; et al. Mesenchymal stem cell-derived exosomes as a nanotherapeutic agent for amelioration of inflammation-induced astrocyte alterations in mice. *Theranostics* **2019**, *9*, 5956. [CrossRef]
60. Wang, Y.; Xu, H.; Wang, J.; Yi, H.; Song, Y. Extracellular vesicles in the pathogenesis, treatment, and diagnosis of spinal cord injury: A mini-review. *Curr. Stem Cell Res. Ther.* **2022**, *17*, 317–327. [CrossRef]
61. Önal, Ö. Sıçanlarda Siklofosfamide Bağlı Ovaryan Toksisitede Yağ Dokudan Elde Edilen Mezenkimal Kök Hücrelerin Pten/Akt/Foxo3a Yolağına Etkisi. 2018. Available online: https://hdl.handle.net/11499/27840 (accessed on 5 December 2024).